

## Waveform $Q$ tomography with central-frequency shifts

Wenyong Pan

### ABSTRACT

Subsurface  $Q$  (quality factor) structures can provide important constraints for characterizing hydrocarbon reservoirs and interpreting tectonic structures and evolution of Earth in exploration and earthquake seismology. The damping effects of attenuation on seismic amplitudes and phases can be modeled based on the generalized standard linear solid (GSLS) rheology. Compared to traditional ray-based methods, full-waveform adjoint tomography is promising to provide more accurate  $Q$  models by numerically solving the viscoelastodynamic wave equation. However, the progress of adjoint  $Q$  tomography is impeded by the difficulties of calculating  $Q$  sensitivity kernels and significant velocity- $Q$  trade-offs. In this study, following the adjoint-state method, I derive the  $Q$  (P- and S-wave quality factors  $Q_P$  and  $Q_S$ ) sensitivity kernels, which can be efficiently constructed with memory strain variables. A new central-frequency difference misfit function is designed to reduce the trade-off artifacts caused by velocity errors for adjoint  $Q$  tomography. Compared to traditional waveform-difference misfit function, this new misfit function is less sensitive to velocity variations and thus can invert for the  $Q$  models more stably suffering fewer trade-off uncertainties.

### INTRODUCTION

As seismic waves propagating in Earth's interior, partial energy is transformed into heat due to intrinsic attenuation, leading to amplitude dissipation and velocity dispersion of the waveforms (Liu et al., 1976). In a linear viscoelastic solid, the attenuation effects are commonly quantified with quality factor  $Q$ . Subsurface  $Q$  variations are associated with permeability, crack density, fluid-saturation, partial melt, chemical composition, temperature, etc of the Earth materials (Mavko and Nur, 1979). In exploration seismology, high-resolution  $Q$  profiles can provide complement constraints for characterizing fluid-filled/gas-Chimney hydrocarbon reservoirs and produce high-fidelity seismic images with the compensation of amplitude loss and phase distortions. In earthquake seismology, joint interpretation of elastic velocities and  $Q$  anomalies can improve our understandings of crust/mantle structures and tectonic evolution.

Traditionally, subsurface  $Q$  models are obtained by ray-based tomography methods with spectral-ratio (Bath, 1974), central-frequency (Quan and Harris, 1997) or  $t^*$  (Eberhart-Phillips and Chadwick, 2002) measurements of the seismic data. However, these ray-based approaches may give inaccurate  $Q$  values in complex geologic areas due to the inaccuracy of forward modeling operators. Anelasticity of the Earth medium can be modeled using a phenomenological model represented mechanically by a combination of springs and dash spots. The system constructed by several parallel standard linear elements is referred to as the generalized standard linear solid (GSLS) rheology (Carcione et al., 1988). Based on the GSLS model, the damping effects of attenuation on propagating waves can be simulated by solving a set of differential equations with the superposition of parallel relaxation mechanisms (Robertsson et al., 1994; Blanch et al., 1995). Theoretically, high-resolution

$Q$  models with arbitrary spatial variations can be reconstructed using full-waveform adjoint tomography, which has emerged as a powerful tool for obtaining subsurface model properties in both exploration and earthquake seismology (Tarantola, 1984; Tromp et al., 2005; Virieux and Operto, 2009).

However, compared to adjoint tomography of elastic velocity structures, the progress of adjoint  $Q$  tomography is significantly lagging behind. A set of difficulties including the complexity of constructing  $Q$  sensitivity kernels and strong multiparameter coupling impede its advances. Effective inversion strategies and algorithms for reliable  $Q$  estimation are still underdeveloped. In this study, I develop an effective formulation for constructing the  $Q$  sensitivity kernels with strain memory variables. A new misfit function measuring central-frequency variation of the seismic data is designed for reliable  $Q$  inversion by reducing the trade-off artifacts caused by velocity errors. Developments of these algorithms are as introduced in the following.

In full-waveform adjoint tomography, the sensitivity kernels can be calculated efficiently by cross-correlating the forward and adjoint wavefields based on the adjoint-state method (Liu and Tromp, 2006). However,  $Q$  has not been explicitly incorporated into the rheological bodies of time domain viscoelastic wave equation. The damping effects are modeled by determining the relaxation parameters through a least-squares inversion to approximate a constant  $Q$  (Bohlen, 2002). This complicates the calculation of  $Q$  sensitivity kernels. In this study, following the adjoint-state method (Liu and Tromp, 2008; Fichtner and van Driel, 2014), I derive the  $Q_P$  and  $Q_S$  sensitivity kernels in viscoelastic medium, which can be calculated efficiently with the strain memory variables. This formulation represents one effective and theoretically complete approach for viscoelastic adjoint tomography.

The problem of interparameter trade-off significantly complicates the multiparameter full-waveform adjoint tomography (Tarantola, 1986; Innanen, 2014; Pan et al., 2016). In viscoelastic media, velocity errors tend to produce strong artifacts in the inverted  $Q$  models, which impedes the progress of adjoint  $Q$  tomography, increases the inversion uncertainties and may produce misleading interpretations for geophysicists (Mulder and Hak, 2009; Keating and Innanen, 2020). Designing specific misfit function represents one effective approach to reduce the trade-off artifacts for reliable  $Q$  inversion. Pan and Innanen (2019) showed that the amplitude-based misfit functions can resolve the  $Q$  anomalies more effectively than traditional waveform-difference (WD) misfit function. They also realized that it is difficult to preserve the seismic amplitudes, which may be influenced by many other factors including transmission/reflection loss, source and receiver coupling, radiation patterns, etc. Seismic attenuation reduces high-frequencies more rapidly than low-frequencies leading to central-frequency downshift of the seismic data (Hauge, 1981). Thus, a new central-frequency difference (CD) misfit function is designed for adjoint  $Q_P$  and  $Q_S$  tomography in this study. The corresponding adjoint source is derived for calculating the  $Q$  sensitivity kernels. Because central-frequency variation is mainly caused by intrinsic attenuation, the new CD misfit function is relatively insensitive to velocity perturbations and amplitude fluctuations. Thus, more accurate  $Q_P$  and  $Q_S$  models can be obtained suffering from fewer trade-off artifacts.

## THEORY AND METHODS

### Viscoelastic sensitivity kernels

We derive the velocity and  $Q$  sensitivity kernels for viscoelastic full-waveform adjoint tomography following the adjoint-state method:

$$\begin{aligned}
 K_{V_P} &= - \int_0^{t'} 2 \left( \rho V_P^2 \delta_{ij} * \partial_t \varepsilon_{kk}^\dagger - W \kappa^R \delta_{ij} \sum_{p=1}^P \tau^{\sigma p} \epsilon_{kk}^{p,\dagger} \right) \varepsilon_{ij} dt, \\
 K_{V_S} &= - \int_0^{t'} 4 \left( \rho V_S^2 * \partial_t \varepsilon_{ij}^\dagger - \rho V_S^2 \delta_{ij} * \partial_t \varepsilon_{kk}^\dagger + \frac{W}{2} \kappa^R \delta_{ij} \sum_{p=1}^P \tau^{\sigma p} \epsilon_{kk}^{p,\dagger} \right) \varepsilon_{ij} dt, \\
 K_{Q_P} &= \frac{V_P^2}{Q_P (V_P^2 - V_S^2)} \int_0^{t'} \left( \kappa^R \delta_{ij} \sum_{p=1}^P \tau^{\sigma p} \epsilon_{kk}^{p,\dagger} \right) \varepsilon_{ij} dt, \\
 K_{Q_S} &= \frac{2}{Q_S} \int_0^{t'} \left( \mu^R \sum_{p=1}^P \tau^{\sigma p} \epsilon_{ij}^{p,\dagger} - \frac{1}{3} \mu^R \delta_{ij} \sum_{p=1}^P \tau^{\sigma p} \epsilon_{kk}^{p,\dagger} \right) \varepsilon_{ij} dt \\
 &\quad - \frac{V_S^2}{Q_S (V_P^2 - V_S^2)} \int_0^{t'} \left( \kappa^R \delta_{ij} \sum_{p=1}^P \tau^{\sigma p} \epsilon_{kk}^{p,\dagger} \right) \varepsilon_{ij} dt,
 \end{aligned} \tag{1a}$$

where  $\varepsilon_{ij}^\dagger$  and  $\epsilon_{ij}^{p,\dagger}$  represent the adjoint strain fields and adjoint memory strain variables, and the coefficient  $W$  is

$$W = \frac{(Q_S - Q_P) V_P^2 V_S^2}{Q_P Q_S (V_P^2 - V_S^2)^2}. \tag{2}$$

The velocity sensitivity kernels  $K_{V_P}$  and  $K_{V_S}$  consist of the terms associated with adjoint stress fields and adjoint memory strain variables, which are different from those in purely elastic media. The  $Q$  sensitivity kernels  $K_{Q_P}$  and  $K_{Q_S}$  are constructed with forward strain fields and adjoint memory strain variables, which characterize the damping effects of seismic waves.

### Central-frequency difference misfit function

Previous studies reveal that when using WD misfit function, small velocity errors can produce strong trade-off artifacts in the inverted  $Q$  models, as both velocity and  $Q$  variations contribute to the waveform residuals. Theoretically, the inverse Hessian accounts for mitigating the trade-offs. However, in truncated-Newton methods, approximating the inverse Hessian with a small number of conjugate gradient iterations shows limited performances to reduce the trade-off artifacts obviously.

Designing specific misfit functions measuring amplitude and central-frequency variations of the seismic data represent one alternative and effective means to reduce the trade-off artifacts without increasing computational cost. Because seismic amplitudes are also influenced by many other factors including instrument responses, radiation patterns, etc, the amplitude-based misfit functions are easily affected by unexpected amplitude fluctuations. In this study, I introduce a new central-frequency difference (CD) misfit function for

adjoint  $Q$  tomography:

$$\chi_{cd}(Q) = \frac{1}{2} \sum_{\mathbf{x}_r} [f_i^c(Q) - f_{i,obs}^c]^2, \quad (3)$$

where  $f_i^c$  and  $f_{i,obs}^c$  indicate the central-frequencies of synthetic and observed seismic data, respectively. I determine central-frequency of the seismic signal by (Berkhout, 1984; Barnes, 1993)

$$f_i^c = \frac{1}{N} \int_0^{+\infty} f \mathcal{A}_i^2(f) df, \quad (4)$$

where  $f$  indicates frequency,  $\mathcal{A}_i$  represents amplitude spectrum of the seismic data and the coefficient  $N$  in the denominator is

$$N = \int_0^{+\infty} \mathcal{A}_i^2(f) df. \quad (5)$$

Variation of the misfit function with respect to  $Q$  perturbation is given by

$$\Delta \chi_{cd}(Q) = \sum_{\mathbf{x}_r} [f_i^c(Q) - f_{i,obs}^c] \Delta f_i^c, \quad (6)$$

where  $\Delta f_i^c$  indicates the variation of central-frequency due to  $Q$  perturbation:

$$\begin{aligned} \Delta f_i^c = & \left[ \int_0^{+\infty} f \mathcal{A}_i(f) df \right] \frac{2\mathcal{R}[\tilde{u}_i(f) \Delta \tilde{u}_i(f)]}{N \mathcal{A}_i(f)} \\ & - \left[ \int_0^{+\infty} f \mathcal{A}_i^2(f) df \int_0^{+\infty} \mathcal{A}_i(f) df \right] \frac{2\mathcal{R}[\tilde{u}_i(f) \Delta \tilde{u}_i(f)]}{N^2 \mathcal{A}_i(f)}, \end{aligned} \quad (7)$$

where  $\tilde{u}_i$  is the synthetic data in frequency domain, the symbol  $\mathcal{R}$  means real part and  $\Delta \tilde{u}_i$  indicates the data variation caused by  $Q$  perturbation. Inserting equation (7) into equation (6) gives:

$$\begin{aligned} \Delta \chi_{cd} = & \sum_{\mathbf{x}_r} [f_i^c - f_{i,obs}^c] \frac{2\mathcal{R}[\tilde{u}_i(f) \Delta \tilde{u}_i(f)]}{N \mathcal{A}_i(f)} \\ & \times \left[ \int_0^{+\infty} f \mathcal{A}_i(f) df - \frac{1}{N} \int_0^{+\infty} f \mathcal{A}_i^2(f) df \int_0^{+\infty} \mathcal{A}_i(f) df \right]. \end{aligned} \quad (8)$$

Thus, the adjoint source for calculating  $Q$  sensitivity kernels using the central-frequency misfit function  $\chi_{cd}$  in frequency domain can be obtained as:

$$\begin{aligned} \tilde{f}_{i,cd}^{s,\dagger}(f) = & \sum_{\mathbf{x}_r} \frac{2\mathcal{R}[\tilde{u}_i(f) (f_i^c - f_{i,obs}^c)]}{N \mathcal{A}_i(f)} \\ & \times \left[ \int_0^{+\infty} f \mathcal{A}_i(f) df - \frac{1}{N} \int_0^{+\infty} f \mathcal{A}_i^2(f) df \int_0^{+\infty} \mathcal{A}_i(f) df \right]. \end{aligned} \quad (9)$$

Because central-frequency of the seismic data is mainly controlled by  $Q$  variations, the new CD misfit function is expected to invert for the  $Q$  models independent of velocity variations and seismic amplitude fluctuations.

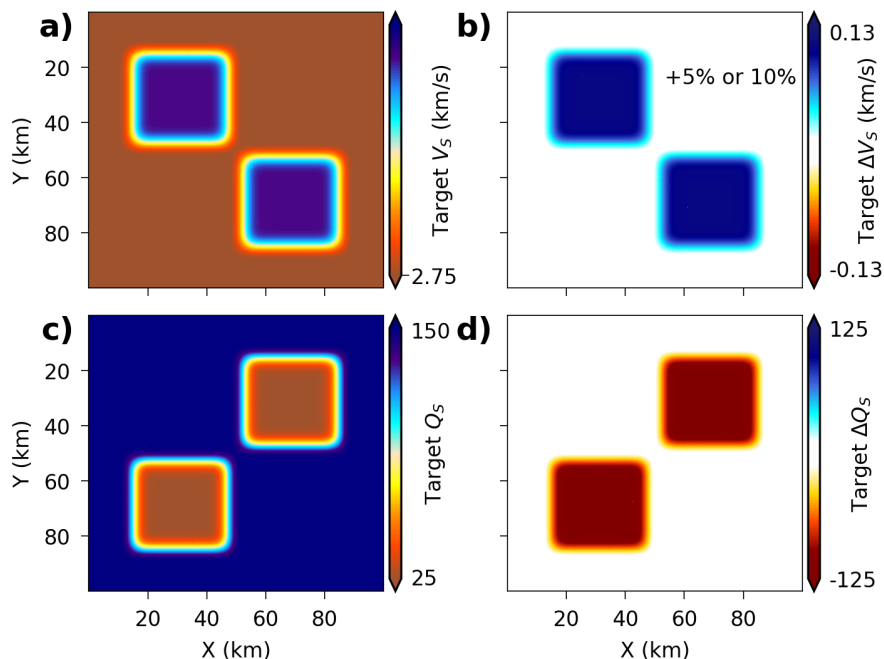


FIG. 1. (a) Acquisition geometry; The red stars and white circles indicate sources and stations, respectively. (b) and (c) are the target  $V_P$  and  $V_S$  velocity models; (d) and (e) are the target  $Q_P$  and  $Q_S$  velocity models.

## NUMERICAL EXPERIMENTS

### Isolated velocity- $Q$ anomaly example

I first design a simple numerical example with isolated velocity and  $Q$  perturbations for testing the effectiveness of the new algorithms. The velocity model is created by embedding two velocity anomalies (+5% or 10% perturbations) in a homogeneous background. The  $V_P/V_S$  ratio is 2. Figures 1a and b show the true  $V_S$  structure and the corresponding model perturbations. The  $Q$  models are created by two strong attenuation anomalies ( $Q_P = Q_S = 25$ ) in a homogeneous background ( $Q_P = Q_S = 150$ ). The velocity and  $Q$  model perturbations are separated for easily visualizing the interparameter mappings.

I first calculated the  $Q_P$  and  $Q_S$  sensitivity kernels ( $K_{Q_P}^{wd}$  and  $K_{Q_S}^{wd}$ ) calculated using traditional WD misfit function with +5% and 10% perturbations, as shown in the first row of Figure 3. As can be seen that velocity errors are mapped into the  $Q$  sensitivity kernels and blur the  $Q$  updates. In the second row of Figure 3, the  $Q_P$  and  $Q_S$  sensitivity kernels ( $K_{Q_P}^{cd}$  and  $K_{Q_S}^{cd}$ ) calculated using the new CD misfit function. The  $Q$  anomalies are clearly imaged with few trade-off artifacts. Figures 4a and b show the inverted  $Q_P$  and  $Q_S$  models using the WD misfit function with +5% velocity perturbations, which are significantly damaged by the mappings from velocity errors. However, when using the new CD misfit function, the inverted  $Q_P$  and  $Q_S$  models suffer from few trade-off artifacts, as shown in Figures 4c and d. These observations suggest that the new CD misfit function can invert for the  $Q$  models more reliably.

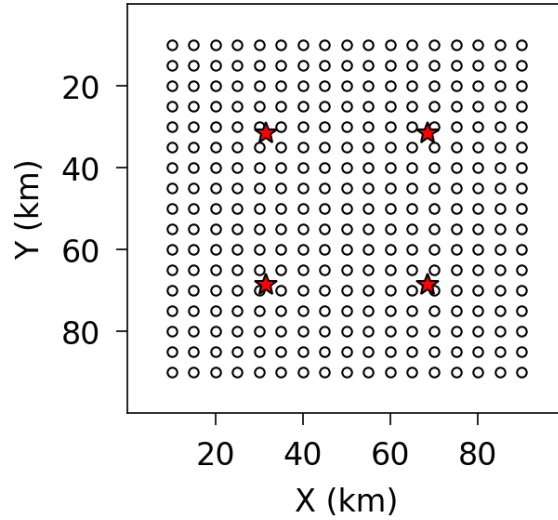


FIG. 2. Acquisition geometry. The red stars and white circles indicate the locations of sources and stations, respectively.

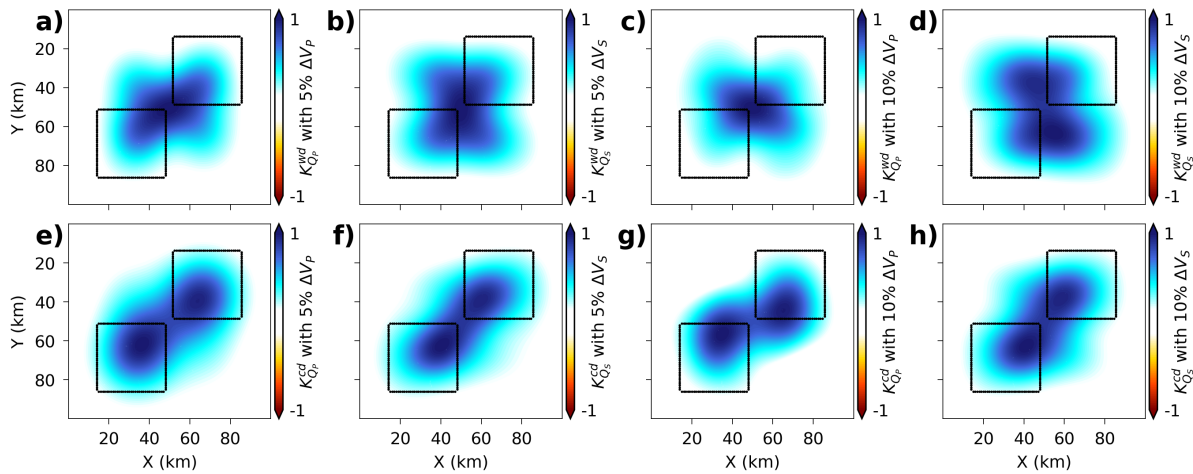


FIG. 3. (a) and (b) are the  $Q_P$  and  $Q_S$  sensitivity kernels  $K_{Q_P}^{wd}$  and  $K_{Q_S}^{wd}$  calculated with WD misfit function and + 5% velocity perturbations; (c) and (d) are the  $Q_P$  and  $Q_S$  sensitivity kernels  $K_{Q_P}^{wd}$  and  $K_{Q_S}^{wd}$  calculated with WD misfit function and + 10% velocity perturbations; (e) and (f) are the sensitivity kernels  $K_{Q_P}^{cd}$  and  $K_{Q_S}^{cd}$  calculated with CD misfit function and + 5% velocity perturbations; (g) and (h) are the sensitivity kernels  $K_{Q_P}^{cd}$  and  $K_{Q_S}^{cd}$  calculated with CD misfit function and + 10% velocity perturbations.

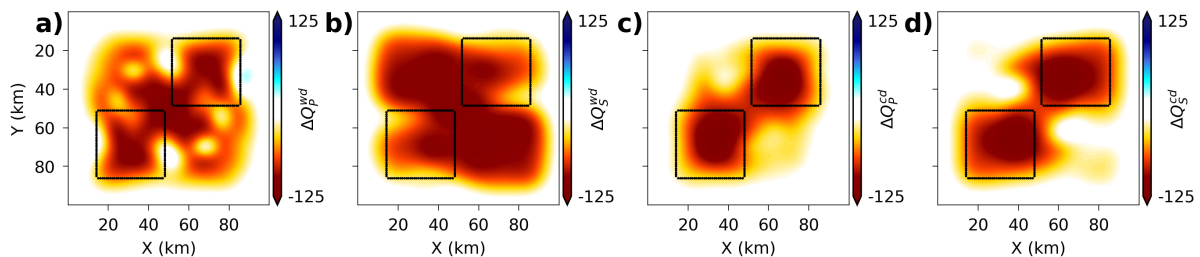


FIG. 4. (a) and (b) are the inverted  $\Delta Q_P^{wd}$  and  $\Delta Q_S^{wd}$  model perturbations using traditional WD misfit function; (c) and (d) are the inverted  $\Delta Q_P^{cd}$  and  $\Delta Q_S^{cd}$  model perturbations using new CD misfit function.

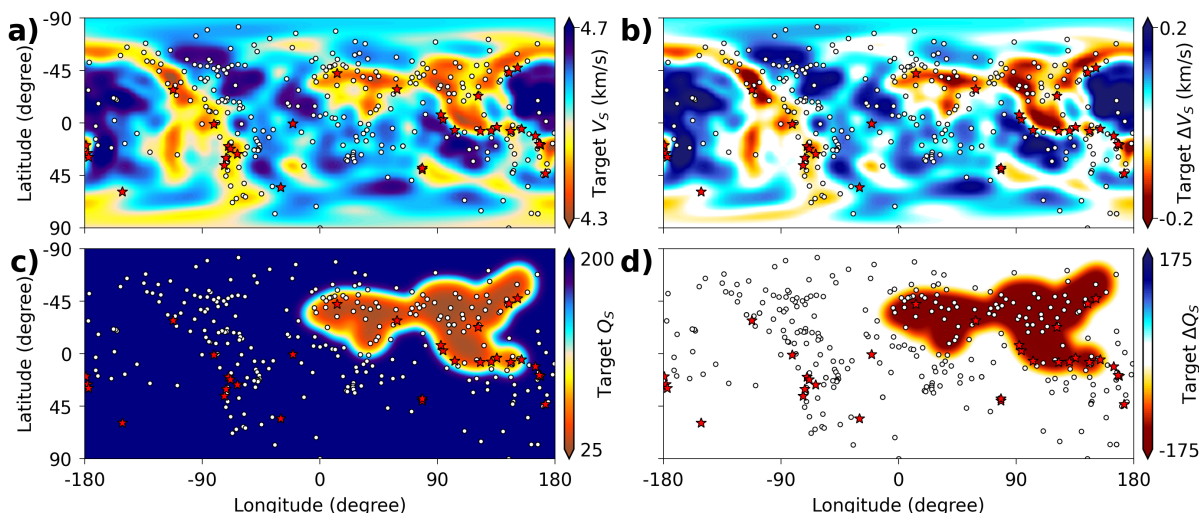


FIG. 5. (a) and (b) are the target  $V_S$  velocity model and corresponding model perturbation  $\Delta V_S$ ; (c) and (d) are the target  $Q_S$  model and corresponding model perturbation  $\Delta Q_S$ . The red stars and white circles indicate the locations of sources and stations.

### Global tomography example

Next, I design a global tomography synthetic example with more realistic structures based on the Rayleigh wave phase speed map provided by Trampert and Woodhouse (1995). Figure 5a shows the target  $V_S$  model. The initial  $V_S$  model is homogeneous with a constant value of 4.5 km/s. Figure 5b shows the target model perturbation  $\Delta V_S$ . The target and initial  $V_P$  models are created with a constant  $V_P/V_S$  of 2. The initial  $Q_S$  model is homogeneous with a constant value of 150. The target  $Q_S$  model is created by embedding one strong attenuation anomaly ( $Q_S = 25$ ) in the homogeneous background, as shown in Figure 5c. Figure 5d shows the target model perturbation  $\Delta Q_S$ . The target and initial  $Q_P$  models are created with  $Q_P = Q_S$ . A number of 32 sources and 293 stations, as indicated by the red stars and white circles in Figure 5a, are distributed in the whole model.

The  $V_P$  and  $V_S$  structures are first inverted in round I. The reconstructed model perturbations  $\Delta V_P$  and  $\Delta V_S$  are presented in Figures 6a and b. Due to the limitation of ray coverage and incorrect  $Q$  models, the inverted velocity structures are not exactly accurate. In round II, the  $Q_P$  and  $Q_S$  models are estimated using the WD and CD misfit functions, respectively. Strong artifacts appear in the inverted  $Q_P$  and  $Q_S$  models using WD misfit function, as shown in Figures 7a and b. The reconstructed  $Q$  anomalies are also distorted. When using the CD misfit function, few artifacts appear in the inverted  $Q_P$  and  $Q_S$  models and the reconstructed  $Q$  anomalies can be clearly identified, as shown in Figures 7c and d.

### 3D viscoelastic FWI example

Finally, I applied the proposed algorithms to invert for near-surface velocity and  $Q$  structures in 3D viscoelastic media with complex topographic variations. Figures 8 and 9 show the true and initial S-wave velocity structures. The true and initial P-wave velocity models are created with  $V_P/V_S = 3$ . Figure 10 shows the true  $Q_S$  model, which is created by embedding the attenuative structure ( $Q_S = 25$ ) in the homogeneous background ( $Q_S =$

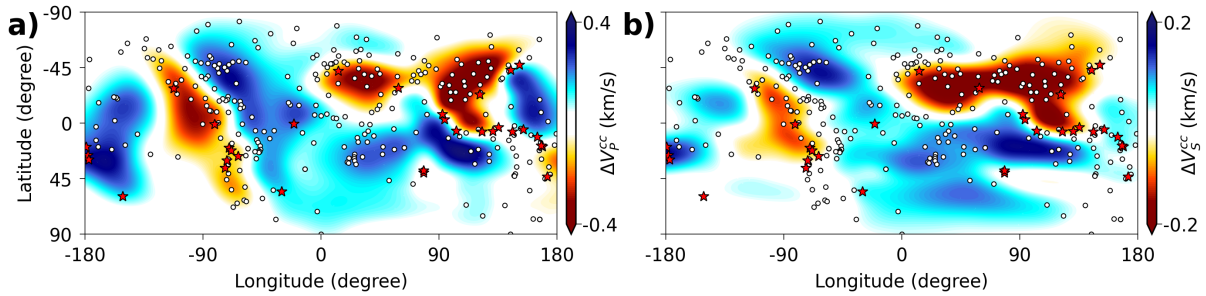


FIG. 6. (a) and (b) are the inverted  $\Delta V_P$  and  $\Delta V_S$  velocity model perturbations.

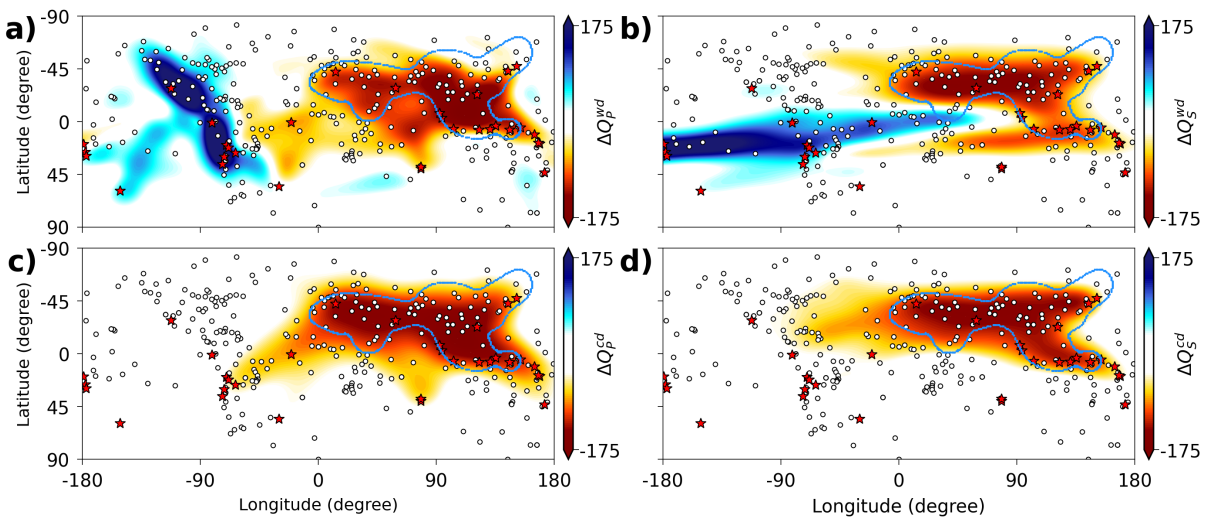
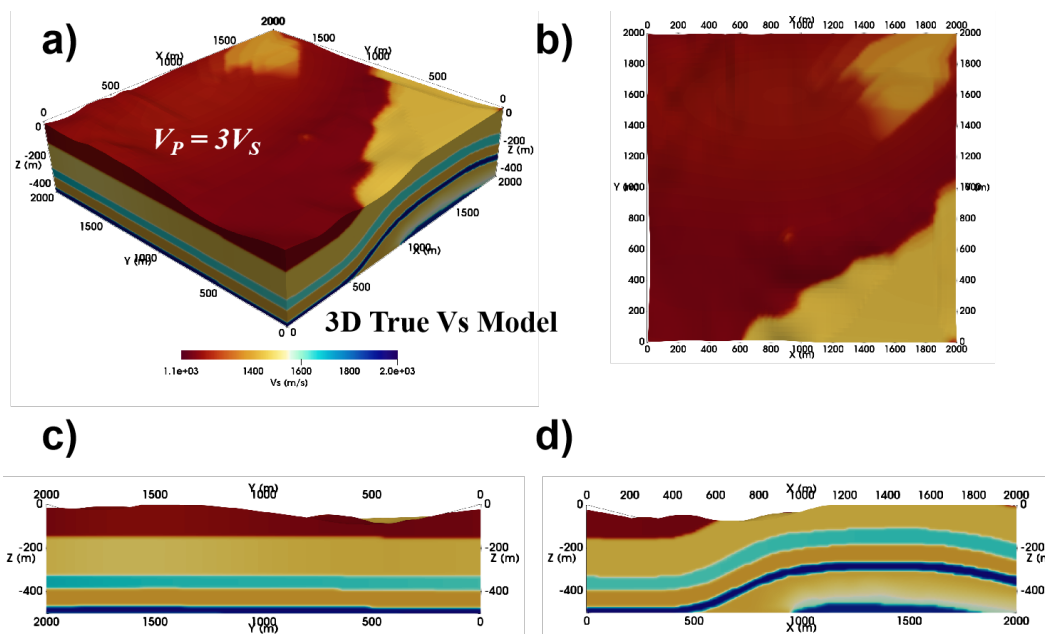


FIG. 7. (a) and (b) are the inverted  $Q$  model perturbations  $\Delta Q_P$  and  $\Delta Q_S$  using the traditional WD misfit function; (c) and (d) are the inverted  $Q$  model perturbations  $\Delta Q_P$  and  $\Delta Q_S$  using the new CD misfit function. The cyan dots depict the boundary of  $Q$  anomalies. The red stars and white circles indicate the locations of sources and stations.

FIG. 8. True 3D  $V_S$  velocity model

200). The initial  $Q_S$  model is homogeneous with  $Q_S = 200$ . The true and initial  $Q_P$  models are created with  $Q_P = Q_S$ . Figure 11 shows the mesh grids for discretizing the model structures and simulating the complex topographic variations. Figures

In round I, the  $V_P$  and  $V_S$  model structures are first estimated. The inversion results are presented in Figures 13 and 14. In round II, the  $Q_P$  and  $Q_S$  models are inverted using the new CD misfit function. Even though, some artifacts appear in the deeper parts of the inverted  $Q_P$  and  $Q_S$  models. The attenuation anomalies at near-surface can be clearly observed suggesting the effectiveness of the proposed algorithm.

## CONCLUSION

In this study, I develop an central-frequency difference misfit function for adjoint  $Q$  tomography. Compared to traditional waveform-difference misfit function, the new approach is almost insensitive to velocity variations and can provide more accurate  $Q$  models suffering from few trade-off artifacts. Effectiveness of the proposed algorithms is verified with synthetic examples.

## REFERENCES

- Barnes, A. E., 1993, Instantaneous spectral bandwidth and dominant frequency with applications to seismic reflection data: *Geophysics*, **58**, No. 3, 419–428.
- Bath, M., 1974, *Spectral analysis in geophysics: Developments in solid earth geophysics*: Elsevier Science Publishing Co.
- Berkhout, A. J., 1984, *Seismic resolution: Resolving power of acoustical echo techniques*: Geophysical Press.
- Blanch, J. O., Robertsson, J. O. A., and Symes, W. W., 1995, *Modeling of a constant Q: Methodology and*

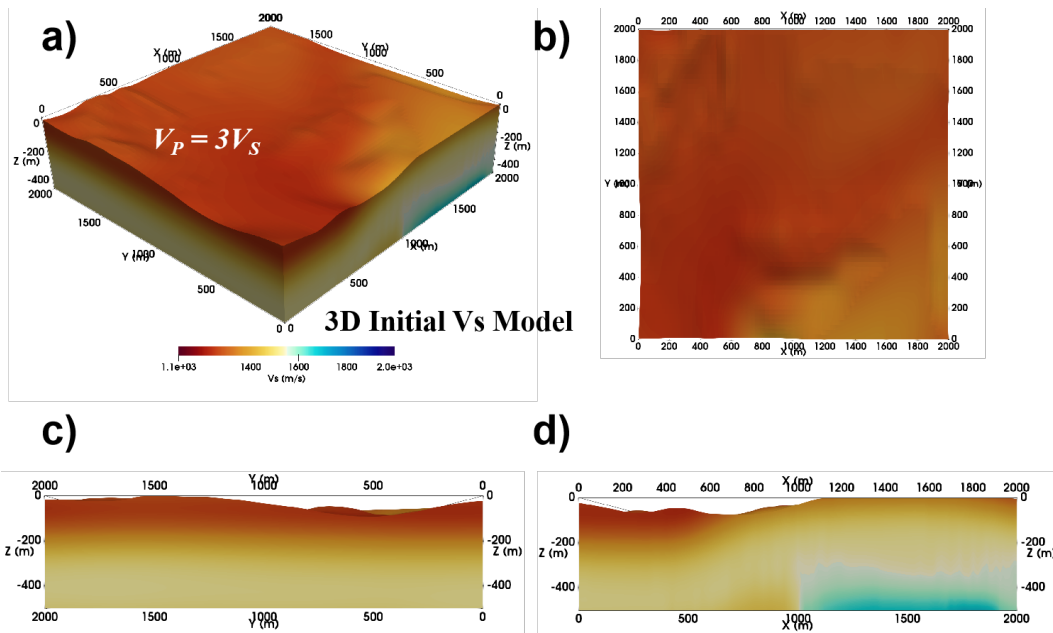


FIG. 9. Initial 3D  $V_S$  velocity model

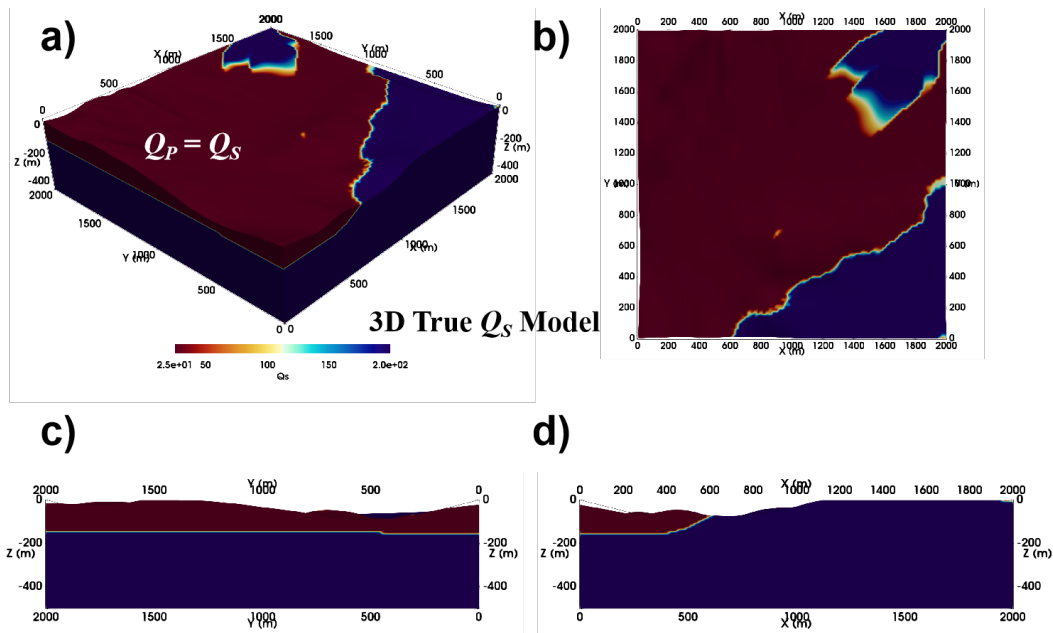


FIG. 10. True 3D  $Q_S$  model.

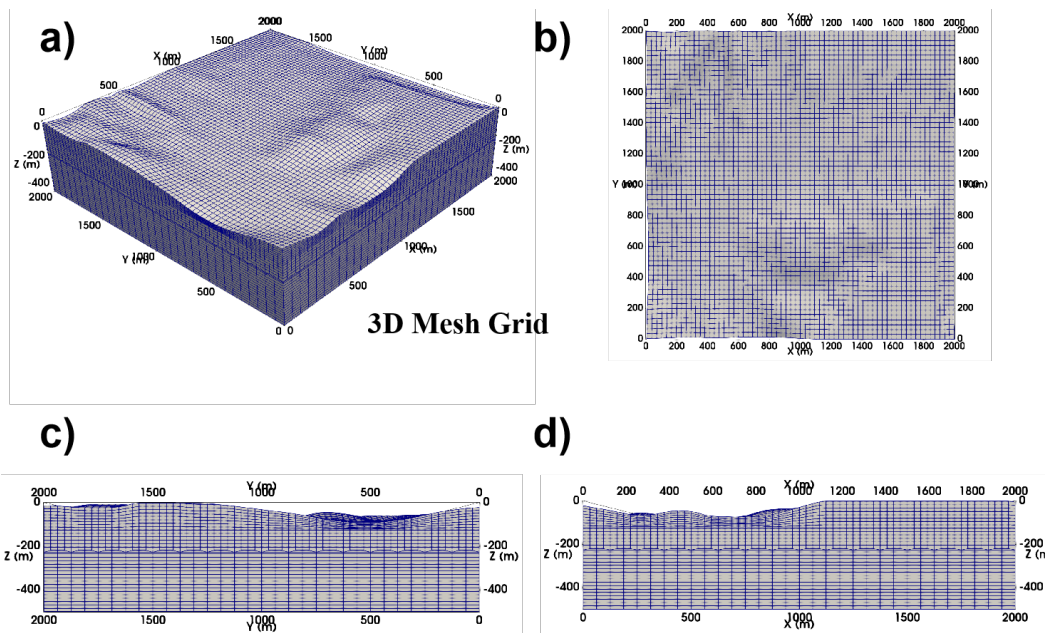


FIG. 11. 3D Mesh grid.

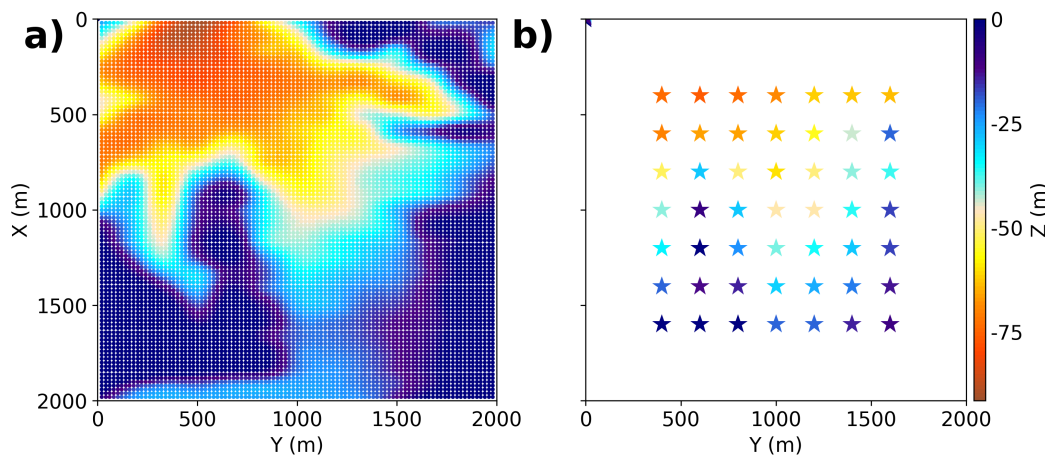


FIG. 12. (a) Locations of the stations; (b) Locations of the sources. Color indicates elevations of the sources and stations.

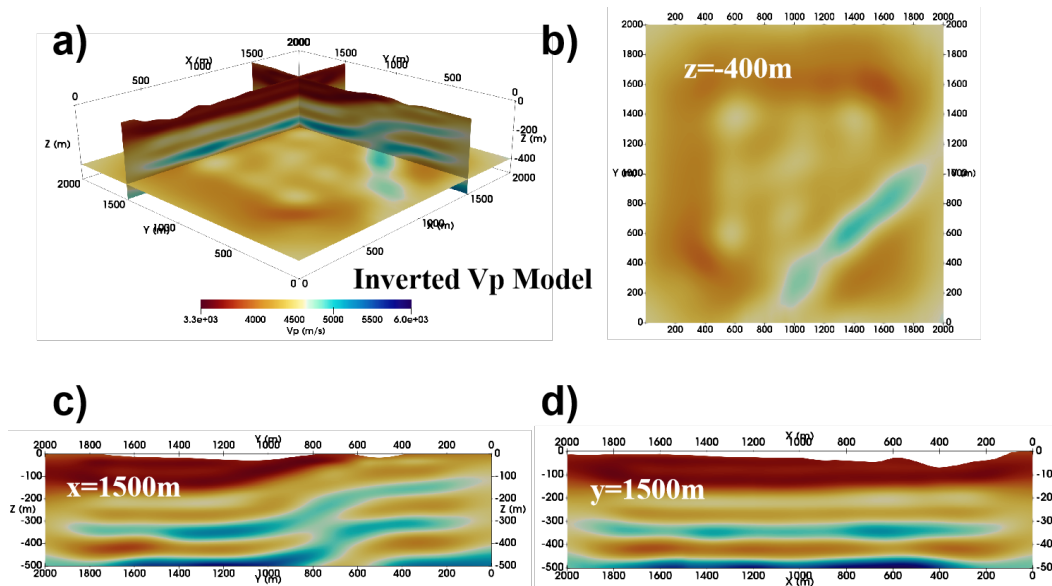


FIG. 13. Inverted 3D  $V_P$  model.

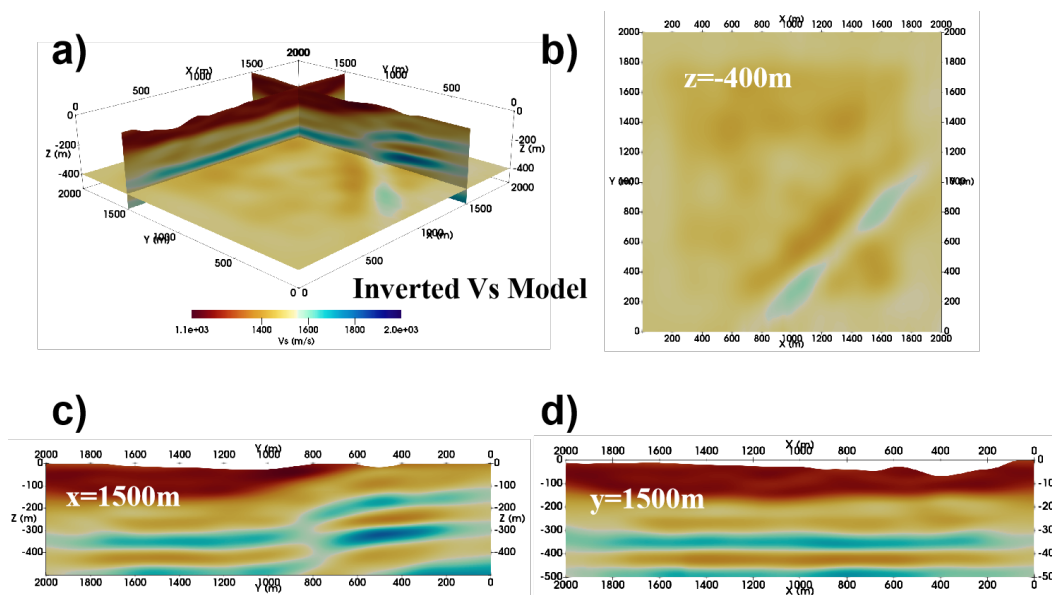


FIG. 14. Inverted 3D  $V_S$  model.

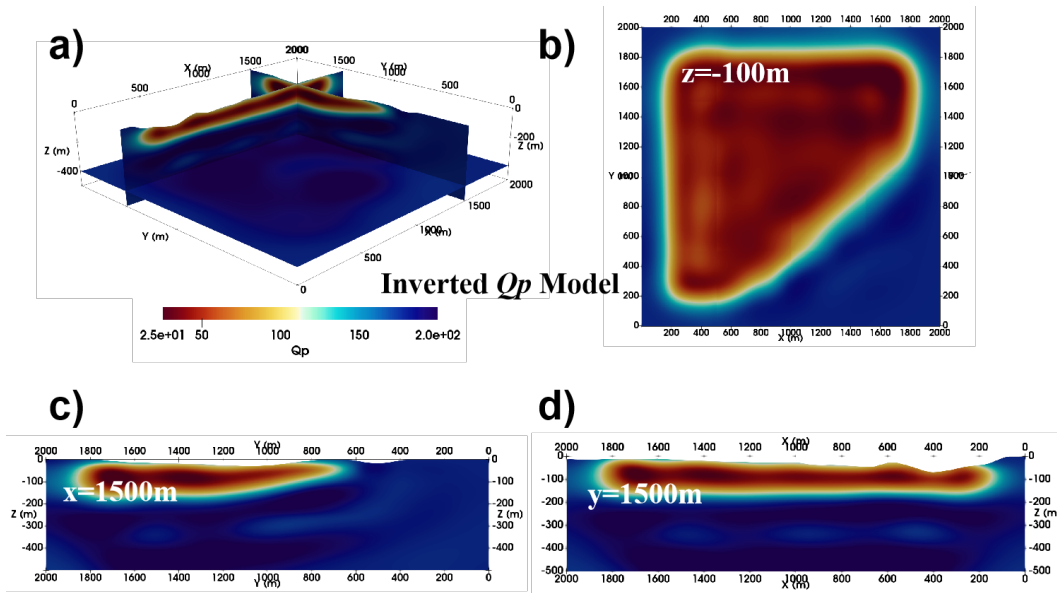


FIG. 15. Inverted 3D  $Q_P$  model.

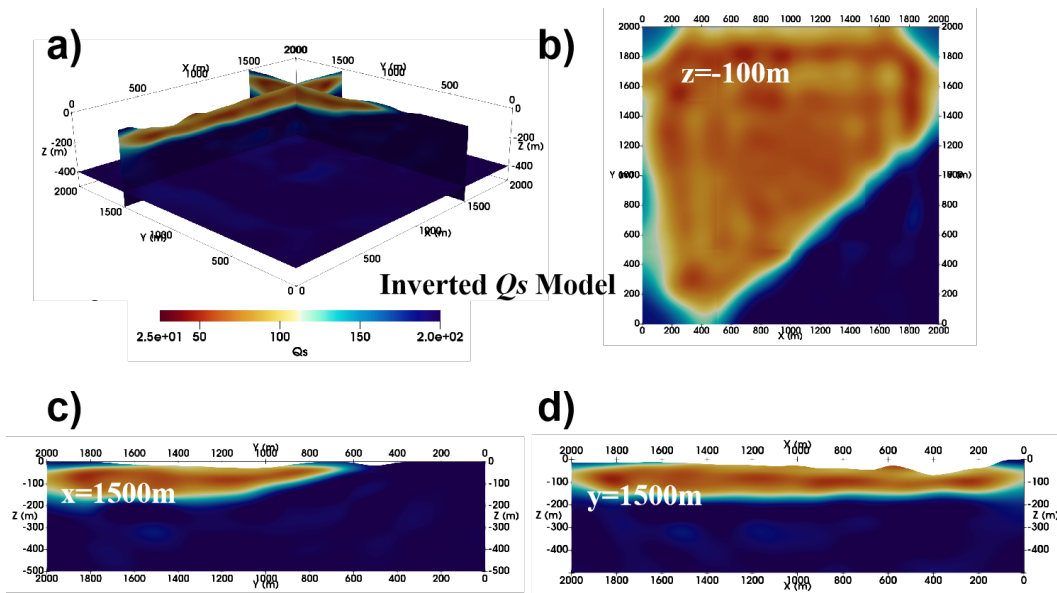


FIG. 16. Inverted 3D  $Q_S$  model.

- algorithm for an efficient and optimally inexpensive viscoelastic technique: *Geophysics*, **60**, No. 1, 176–184.
- Bohlen, T., 2002, Parallel 3-D viscoelastic finite difference seismic modelling: *Computer & Geosciences*, **28**, 845–870.
- Carcione, J. M., Kosloff, D., and Kosloff, R., 1988, Viscoacoustic wave propagation simulation in the earth: *Geophysics*, **53**, 769–777.
- Eberhart-Phillips, D., and Chadwick, M., 2002, Three-dimensional attenuation model of the shallow Hikurangi subduction zone in the Raukumara Peninsula, New Zealand: *J. Geophys. Res.*, **107**, No. B2, 2033.
- Fichtner, A., and van Driel, M., 2014, Models and Fréchet kernels for frequency-(in)dependent Q: *Geophysical Journal International*, **198**, 1878–1889.
- Hauge, P., 1981, Measurements of attenuation from vertical seismic profiles: *Geophysics*, **46**, 1548–1558.
- Innanen, K. A., 2014, Seismic AVO and the inverse Hessian in precritical reflection full waveform inversion: *Geophysical Journal International*, **199**, 717–734.
- Keating, S., and Innanen, K. A., 2020, Parameter crosstalk and leakage between spatially separated unknowns in viscoelastic full-waveform inversion: *Geophysics*, **85**, No. 4, R397–R408.
- Liu, H., Anderson, D. L., and Kanamori, H., 1976, Velocity dispersion due to anelasticity; implications for seismology and mantle composition: *Geophys. J. R. Astron. Soc.*, **47**, No. 1, 41–58.
- Liu, Q., and Tromp, J., 2006, Finite-Frequency Kernels Based on Adjoint Methods: *Bulletin of Seismological Society of America*, **96**, No. 6, 2383–2397.
- Liu, Q., and Tromp, J., 2008, Finite-frequency sensitivity kernels for global seismic wave propagation based upon adjoint methods: *Geophysical Journal International*, **174**, 265–286.
- Mavko, G. M., and Nur, A., 1979, Wave attenuation in partially saturated rocks: *Geophysics*, **44**, No. 0, 161–178.
- Mulder, W. A., and Hak, B., 2009, An ambiguity in attenuation scattering imaging: *Geophysical Journal International*, **178**, 1614–1624.
- Pan, W., and Innanen, K. A., 2019, Amplitude-based misfit functions in viscoelastic full-waveform inversion applied to walk-away vertical seismic profile data: *Geophysics*, **84**, No. 5, B335–B351.
- Pan, W., Innanen, K. A., Margrave, G. F., Fehler, M. C., Fang, X., and Li, J., 2016, Estimation of elastic constants for HTI media using Gauss-Newton and full-Newton multiparameter full-waveform inversion: *Geophysics*, **81**, No. 5, R275–R291.
- Quan, Y., and Harris, J. M., 1997, Seismic attenuation tomography using the frequency shift method: *Geophysics*, **62**, 895–905.
- Robertsson, J. O., Blanch, J. O. A., and Symes, W. W., 1994, Viscoelastic finite-difference modeling: *Geophysics*, **59**, 1444–1456.
- Tarantola, A., 1984, Inversion of seismic reflection data in the acoustic approximation: *Geophysics*, **49**, 1259–1266.
- Tarantola, A., 1986, A strategy for nonlinear elastic inversion of seismic reflection data: *Geophysics*, **51**, 1893–1903.
- Trampert, J., and Woodhouse, J. H., 1995, Global phase-velocity maps of Love and Rayleigh-waves between 40 and 150 seconds: *Geophysical Journal International*, **122**, No. 2, 675–690.
- Tromp, J., Tape, C., and Liu, Q., 2005, Seismic tomography, adjoint methods, time reversal, and banana-doughnut kernels: *Geophysical Journal International*, **160**, 195–216.
- Virieux, A., and Operto, S., 2009, An overview of full-waveform inversion in exploration geophysics: *Geophysics*, **74**, No. 6, WCC1–WCC26.